# Explicit Green's function of a boundary value problem for a sphere and trapped flux analysis in Gravity Probe B experiment

I. M. Nemenman[a] and A. S. Silbergleit
*Gravity Probe B, W. W. Hansen Experimental Physics Laboratory, Stanford University, Stanford, California 94305-4085*

(Received 25 January 1999; accepted for publication 1 April 1999)

Magnetic flux trapped on the surface of superconducting rotors of the Gravity Probe B (GP-B) experiment produces some signal in the superconducting quantum interference device readout. For the needs of GP-B error analysis and simulation of data reduction, this signal is calculated and analyzed in this article. We first solve a magnetostatic problem for a point source on the surface of a sphere, finding the closed form elementary expression for the corresponding Green's function. Second, we calculate the flux through the pick-up loop as a function of the source position. Next, the time dependence of a source position, caused by rotor motion according to a symmetric top model, and thus the time signature of its flux are determined, and the spectrum of the trapped flux signal is analyzed. Finally, a multipurpose program of trapped flux signal generation based on the above results is described, various examples of the signal obtained by means of this program are given, and their features are discussed. Signals of up to 100 fluxons, i.e., 100 pairs of positive and negative point sources, are examined. © *1999 American Institute of Physics.* [S0021-8979(99)08113-X]

## I. INTRODUCTION

The Gravity Probe B (GP-B) satellite is scheduled to fly in the year 2000. It contains a set of gyroscopes intended to test the predictions of general relativity that a gyroscope in a low (altitude ≈650 km) circular polar orbit will precess, relative to a distant star, about 6.6 arcsec/year in the orbital plane (DeSitter, or geodetic, precession) and about 42 marcsec/year perpendicular to the orbital plane (Lense–Thirring, or frame-dragging, precession). To provide the desired measurement accuracy (1 part in $10^5$ for the geodetic effect), a magnetic London moment readout using a superconducting quantum interference device (SQUID) has been chosen, so that the experiment will be carried out at low temperature (~2.5 K), and the gyrorotors will be superconducting (see Refs. 1, 2, and 3 for the design and status of the experiment; the history of GP-B development is found in Ref. 4, and a survey of space relativity tests is in Ref. 5). The direction of the magnetic London moment developed in a rotating superconductor coincides with the direction of the rotation (spin) axis[6] (for basic superconductor physics see Ref. 7; the description of gyromagnetic effects can be found in Ref. 8). The corresponding magnetic flux through the pick-up loop of the SQUID is proportional to the sine of the angle between the London moment vector and the pick-up loop plane, so the change of this angle, and thus the drift of the gyroscope axis, can be detected from the SQUID signal at the roll frequency of the spacecraft which will be deliberately rotated.

However, along with the London moment dipole, there will also be quantum-size sources of magnetic field pinned to the surface of the superconducting rotor (see Refs. 7 and 9). They appear in pairs of the opposite polarity called fluxons; the sources constituting the pair are connected by a magnetic vortex line going through the whole body of the superconductor (see Fig. 1). The fluxons produce additional magnetic flux through the pick-up loop called trapped flux; its time signature will be present in the SQUID output. The low frequency part of this signal, although comparatively small under the GP-B conditions, might corrupt the accuracy of the London moment readout. On the other hand, its high frequency part can provide additional information that is significant for the experimental results. To make sure the trapped flux does not affect the measurement precision, as well as to extract useful information from it, one has to analyze the trapped flux signal and develop the code generating it for the use in simulations of the GP-B error analysis and data reduction. This is the primary goal of the present article; we also hope that our analysis may be of use for other applications as well. Note that the first work on the analysis of the trapped flux from a GP-B rotor was done by Wai in his thesis.[10]

In Sec. II we give a closed form solution to a magnetostatic problem of a point field source (''magnetic charge,'' ''half-fluxon'') on the surface of the gyroscope. In Sec. III the solution is used to find the trapped flux signal in the pick-up loop as a function of the half-fluxon's position. The closed form expression for the trapped flux appears to be not very useful for further applications, so various exact and approximate formulas are also obtained. In Sec. IV we investigate the motion of fluxons with respect to the pick-up loop, thus finding the time signature of the trapped flux signal; we then go on to analyze its frequency spectrum. Section V contains a brief description of the program used to simulate

[a]Permanent address: Department of Physics, Princeton University, Princeton, NJ 08544; electronic mail: nemenman@princeton.edu

 

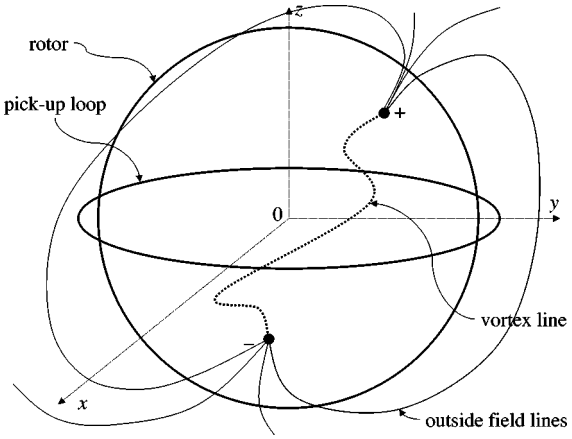


FIG. 1. Rotor with a fluxon.

trapped flux for the GP-B data processing routines. Pictures of the high frequency signal, its low frequency envelope, and various Fourier spectra are presented and discussed.

## II. THE GREEN'S FUNCTION OF THE MAGNETOSTATIC PROBLEM

The GP-B experiment will be conducted at low temperatures, so the fluxons can be treated as static (welded to the rotor's surface) and noninteracting ones. In such a case the total fluxon field is a superposition of the fields of individual fluxons, each consisting of contributions from its positive and negative magnetic charges. In addition, the rate of change of this field due to the rotor's motion is negligible, hence the magnetostatic approach should be used. Thus we consider a single (positive) source of the field whose characteristic size is on the order of $10^{-5}$ cm;[9] due to a macroscopic size of the gyroscope (1.91 cm radius), this can be treated as a point source of magnetic field with the coordinate angles $\vartheta_+$, $\varphi_+$ on the surface $r=r_g$ of the rotor. The spherical coordinates $r,\vartheta,\varphi$ here correspond to a Cartesian frame $\{x,y,z\}$ fastened to the pick-up loop so that the origin coincides with the loop center and the $z$ axis is perpendicular to the loop plane; the real relative motion of the fluxon and the loop, i.e., the dependence of the position angles $\vartheta_+$, $\varphi_+$ on time, will be incorporated and examined in Sec. IV.

In these settings, the boundary value problem for the magnetic potential $\Psi(\mathbf{r})$ of the fluxon outside the rotor is formulated as

$$\Delta\Psi(\mathbf{r})=0, \quad r>r_g,\ 0\leqslant\theta_+\leqslant\pi,\ 0\leqslant\varphi_+<2\pi, \tag{1}$$

$$-\left.\frac{\partial\Psi}{\partial r}\right|_{r=r_g}=\frac{\Phi_0}{r_g^2\sin\vartheta_+}\,\delta(\vartheta-\vartheta_+)\,\delta(\varphi-\varphi_+), \tag{2}$$

where $\Phi_0=h/2e$ is the magnetic flux quantum, and the magnetic field is

$$\mathbf{B}=-\nabla\Psi. \tag{3}$$

Evidently, up to a factor $\Phi_0$, $\Psi$ is the Green's function of the external Neumann boundary value problem for a sphere.

A standard separation of variables leads to the following series representation of the solution to Eqs. (1) and (2):

$$\Psi(\mathbf{r})\equiv\Psi(r,\vartheta,\varphi)=\frac{\Phi_0}{2\pi r_g}\sum_{l=0}^{\infty}\sum_{m=0}^{l}(M_{lm}\cos m\varphi + N_{lm}\sin m\varphi)\left(\frac{r_g}{r}\right)^{l+1}P_l^m(\cos\vartheta), \tag{4}$$

with the coefficients given by

$$M_{lm}=\frac{2l+1}{(1+\delta_{m0})(l+1)}\,\frac{(l-m)!}{(l+m)!}P_l^m(\cos\vartheta_+)\cos m\varphi_+,$$
$$N_{lm}=\frac{2l+1}{(l+1)}\,\frac{(l-m)!}{(l+m)!}P_n^m(\cos\vartheta_+)\sin m\varphi_+. \tag{5}$$

As it turns out, this series may be summed to give the closed form solution for $\Psi$. To determine it, we first introduce Eq. (5) into Eq. (4) to obtain

$$\Psi(\mathbf{r})=\frac{\Phi_0}{4\pi r_g}\sum_{l=0}^{\infty}\frac{2l+1}{l+1}\left(\frac{r_g}{r}\right)^{l+1}\left[P_l(\cos\vartheta)P_l(\cos\vartheta_+)+2\sum_{m=0}^{l}P_l^m(\cos\vartheta)P_l^m(\cos\vartheta_+)\cos m(\varphi-\varphi_+)\right].$$

Then, by applying the addition theorem for Legendre functions [see Ref. 11 (10.11), (47)], we convert the latter into

$$\Psi(\mathbf{r})=\frac{\Phi_0}{4\pi r_g}\sum_{l=0}^{\infty}\frac{2l+1}{l+1}\left(\frac{r_g}{r}\right)^{l+1}P_l(\cos\gamma)$$
$$=\frac{\Phi_0}{4\pi r_g}\left[2\sum_{l=0}^{\infty}\left(\frac{r_g}{r}\right)^{l+1}P_l(\cos\gamma)-\sum_{l=0}^{\infty}\frac{1}{l+1}\left(\frac{r_g}{r}\right)^{l+1}P_l(\cos\gamma)\right], \tag{6}$$

where $\gamma$ is the angle between the directions to the fluxon and to the observer

$$\cos\gamma\equiv\cos\vartheta\cos\vartheta_+ + \sin\vartheta\sin\vartheta_+\cos(\varphi-\varphi_+). \tag{7}$$

The first of the series in the above expression for $\Psi$ is obviously the generating function for Legendre polynomials [see Ref. 11 (10.10), (39)], the second one is just an integral of it, namely,

$$\sum_{l=0}^{\infty}\frac{1}{l+1}\eta^{l+1}P_l(\zeta)=\int_0^{\eta}d\tau\sum_{l=0}^{\infty}\tau^lP_l(\zeta)$$
$$=\int_0^{\eta}\frac{d\tau}{\sqrt{1-2\zeta\tau+\tau^2}}$$
$$=\ln\frac{\eta-\zeta+\sqrt{1-2\zeta\eta+\eta^2}}{1-\zeta}.$$

Using these results in Eq. (6), we can now write the magnetic potential in its final form as a finite combination of elementary functions,

$$\Psi(\mathbf{r}) \equiv \Phi_0\, G(\mathbf{r},\mathbf{r}_+) = \frac{\Phi_0}{2\pi}\left[\frac{1}{|\mathbf{r}-\mathbf{r}_+|} - \frac{1}{2r_g}\ln\frac{r_g^2 - \mathbf{r}\cdot\mathbf{r}_+ + r_g|\mathbf{r}-\mathbf{r}_+|}{rr_g - \mathbf{r}\cdot\mathbf{r}_+}\right], \quad (8)$$

where $G(\mathbf{r},\mathbf{r}_+)$ is the Green function mentioned and $\mathbf{r}_+ = \{r_g, \vartheta_+, \varphi_+\}$ is the position vector of the source. The first term here, as one would expect, is a half of the potential of a point charge, and the addition to it describes the contribution of the curved boundary.

Since, surprisingly enough, we were not able to find this explicit formula in the literature, it seems reasonable to give here a closed form expression for the Green function of the corresponding Dirichlet problem ($G_0$), in which boundary condition (2) is replaced by

$$\Psi|_{r=r_g} = \frac{\Phi_0}{r_g \sin\vartheta_+}\,\delta(\vartheta-\vartheta_+)\,\delta(\varphi-\varphi_+). \quad (9)$$

The result then is

$$\Psi(\mathbf{r}) \equiv \Phi_0\, G_0(\mathbf{r},\mathbf{r}_+) = \frac{\Phi_0}{4\pi}\,\frac{r^2-r_g^2}{|\mathbf{r}-\mathbf{r}_+|^3}. \quad (10)$$

Note that the Green's functions for the corresponding internal problems can be obtained from Eqs. (8) and (10) by means of inversion.

## III. TRAPPED FLUX AS A FUNCTION OF A MAGNETIC CHARGE POSITION

Magnetic flux measured by the pick-up loop of a GP-B SQUID is the flux through the circle of the radius $R$ in the plane $z=0$, or, equivalently, the flux through the (upper) hemisphere. The dependence of the trapped flux on the half-fluxon position turns out to be rather complicated, especially for the GP-B design, when the gap between the rotor and the loop is very small as compared to the pick-up loop radius $R$. For that reason we give here a number of different representations of the trapped flux as a function of the fluxon position; each of them has its own merits and drawbacks and is thus used for different purposes pertinent to our investigation.

### A. Trapped flux in terms of a series of Legendre polynomials

The simplest way to calculate the trapped flux is to integrate over the hemisphere the series expression for the radial component of the magnetic field obtained from Eqs. (3)–(5):

$$\Phi_+ = \int_{\text{hemisphere }(r=R)} B_r\Big|_{r=R}\, dA = \int_{\text{hemisphere }(r=R)} -\frac{\partial\Psi}{\partial r}\Big|_{r=R}\, dA = \Phi_0 \sum_{l=0}^{\infty} (l+1)\left(\frac{r_g}{R}\right)^l M_{l0}\int_0^1 P_l(s)\, ds;$$

all spherical harmonics with $m\neq 0$ here have averaged out over the azimuthal angle $\varphi$. The last integral is calculated with the help of the known relations of the theory of Legendre polynomials [see Ref. 11 (10.10), (14), (2), (4)]:

$$P_l(s) = \frac{P'_{l+1}(s) - P'_{l-1}(s)}{l+1}; \quad P_l(1) = 1;$$

$$P_{2k+1}(0) = 0; \quad P_{2k}(0) = \frac{(-1)^k}{\sqrt{\pi}}\,\frac{\Gamma(k+1/2)}{k!};$$

$$l,k = 0,1,\ldots;$$

$\Gamma(\zeta)$ is the Euler gamma function. Then, after inserting the values $M_{l0}$ from Eq. (5), we arrive at the following expressions:

$$\Phi_+(\cos\vartheta_+) = \frac{\Phi_0}{2} F_\delta(\cos\vartheta_+);$$

$$F_\delta(s) = \sum_{k=0}^{\infty} (1-\delta)^{2k+1} P_{2k+1}(s)[P_{2k}(0) - P_{2k+2}(0)] = \frac{2}{\sqrt{\pi}}\sum_{k=0}^{\infty}(-1)^k \frac{k+3/4}{(k+1)!}\Gamma(k+1/2) \times (1-\delta)^{2k+1} P_{2k+1}(s). \quad (11)$$

Here $\delta$ denotes the dimensionless gap between the pick-up loop and the rotor, $0 \leqslant \delta = (R-r_g)/R < 1$.

From the point of view of signal processing, $F_\delta(s)$ is a transfer function which converts the ''input'' half-fluxon position signal $S_{\text{in}}(t) = \cos\vartheta_+(t)$ (the position is changing with time as the rotor moves relative to the pick-up loop; see Sec. IV), into an ''output'' trapped flux signal $S_{\text{out}}(t) = 0.5\Phi_0 F_\delta[S_{\text{in}}(t)]$ which is present in the GP-B readout. Since the total contribution to the flux of any number of fluxons scattered in any way over the rotor's surface is given by the sum of the values of the same function $F_\delta$ taken at proper different values of its argument, it was called ''universal curve'' in Ref. 10. Clearly, $F_\delta(s)$ is an odd function of $s$; in particular, $F_\delta(0) = 0$ means that a source sitting exactly in the pick-up loop plane does not, of course, register any flux.

By setting $\delta = 0$ in Eq. (11) (the loop on the surface of the rotor), we immediately find

$$F_0(s) = \frac{2}{\sqrt{\pi}}\sum_{k=0}^{\infty}(-1)^k\frac{k+3/4}{(k+1)!}\Gamma(k+1/2)P_{2k+1}(s) = \begin{cases} 1 & \text{if } 0 < s \leqslant 1; \\ 0 & \text{if } s = 0; \\ -1 & \text{if } -1 \leqslant s < 0 \end{cases} \quad (12)$$

(the last equality here is proved by expanding its right-hand side in the orthogonal series of Legendre polynomials).

This result obtained by Wai[10] has a clear physical meaning: when the pick-up loop lies on the rotor's surface, the same as the point source of field always does, the flux through the loop remains unchanged ($\pm\Phi_0/2$, half of the total) while the half-fluxon stays in either of the hemispheres separated by the plane of the loop, and changes its sign by a jump when the half-fluxon crosses this plane. However, Eq.

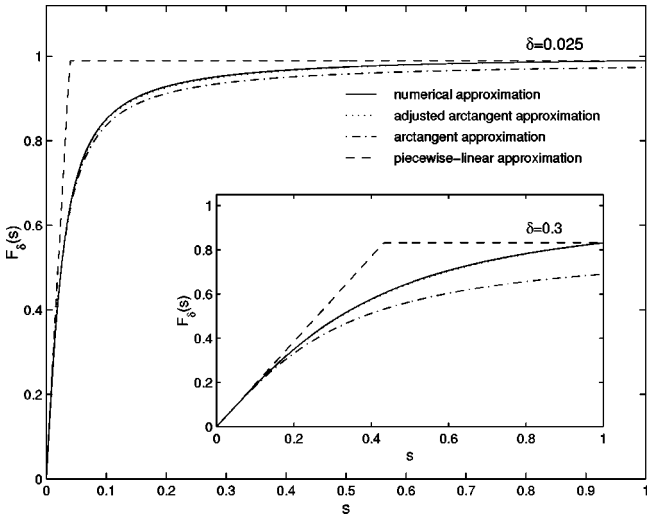


FIG. 2. Universal curve $F_\delta(s)$.

(12) also demonstrates the difficulties in using expression (11) for GP-B, where $\delta=0.025$ is very small: for any $\delta>0$ the series of Eq. (11) has an absolutely converging majorant, so its sum $F_\delta(s)$ is an analytical function of $s$, but it has a jump discontinuity at $s=0$ when $\delta=0$. Therefore the series of Eq. (11) converges worse and worse with the separation $\delta$ becoming smaller and smaller, which makes Eq. (11) practically unacceptable for accurate numerical calculations at the required value of separation. It also turns finding *a uniform in s* asymptotic expansion of $F_\delta(s)$ for $\delta\to 0$ into a rather difficult mathematical problem. The effect is that for small positive values of $\delta$ the transfer function has the shape of a very steep ''kink'' [recall that $F_\delta(s)$ is odd]: it is almost constant outside a small vicinity $(-\Delta_\delta, \Delta_\delta)$ of the origin, with $\Delta_\delta=O(\delta)$ as shown below, and is equal to zero at $s=0$ with a huge gradient $\sim O(1/\delta)$ there (see Fig. 2). That is why we are deriving three more representations for $F_\delta(s)$ in the text that follows.

### B. Integral representation of the trapped flux

An integral expression for $F_\delta(s)$ is obtained by replacing the Legendre polynomials in Eq. (11) by their integral representation [see Ref. 11 (10.10), (43)]

$$P_{2k+1}(\cos\vartheta_+)=\frac{1}{\pi}\int_{-\vartheta_+}^{\vartheta_+}\frac{\exp[i(2k+1+1/2)]\,d\psi}{\sqrt{2(\cos\psi-\cos\vartheta_+)}}.$$

Changing then the order of summation and integration, we arrive at a sum of two hypergeometric series which are readily summed up to result in

$$F_\delta(\cos\vartheta_+)=\frac{\Phi_0\sqrt{2}}{\pi}\int_0^{\vartheta_+}\frac{d\psi\exp(i\psi/2)}{\sqrt{\cos\psi-\cos\vartheta_+}}\times\left[\frac{\lambda}{\sqrt{1+\lambda^2}}-\frac{\sqrt{1+\lambda^2}}{2\lambda}+\frac{1}{2\lambda}\right],\qquad(13)$$

$\lambda\equiv(1-\delta)\exp(i\psi)$.

Representation (13) is very convenient for precise numerical calculation (and, in fact, is used for this purpose in our code; see Sec. V), because the integrand in Eqs. (13) is an algebraic one, and the weak singularity at the upper limit can be taken care of rather easily. The plot of the transfer function computed from Eqs. (13) is given in Fig. 2, along with graphs of its various approximations that are described in Sec. III C. The relative error of the numerical computation has been kept within $10^{-5}$.

### C. Elementary approximations of the trapped flux

From the described behavior of $F_\delta(s)$ for small $\delta$ it is clear that to effectively approximate it one needs the value of its gradient at $s=0$ and the ''saturation'' value $F_\delta(1)$ in the first place. Fortunately, it is possible to compute these quantities exactly, and they are

$$f_\delta\equiv F_\delta(1)=\frac{1}{1-\delta}\left[1-\frac{2\delta-\delta^2}{\sqrt{1+(1-\delta)^2}}\right]=1-(\sqrt{2}-1)\delta+O(\delta^2);\qquad(14)$$

$$\kappa_\delta\equiv\left.\frac{\partial F_\delta(s)}{\partial s}\right|_{s=0}=\frac{2}{\pi}\left[\frac{1+(1-\delta)^2}{1-(1-\delta)^2}\mathbf{E}(1-\delta)-\mathbf{K}(1-\delta)\right]=\frac{2}{\pi}\left[\frac{1}{\delta}+2+O(\delta\log\delta^{-1})\right],\quad\delta\to 0;\qquad(15)$$

here $\mathbf{K}(k), \mathbf{E}(k)$ are complete elliptic integrals of the first and second kind, respectively (see Ref. 14 for their definitions and asymptotic behavior at $k\to 1-0$). The formulas are derived from Eq. (11) by direct summation of the corresponding series of Legendre polynomials carried out in the Appendix.

The simplest approximation of the transfer function for $\delta\to+0$ is evidently a piecewise-linear one,

$$F_\delta(s)\approx\begin{cases}1, & \text{if } \Delta_\delta<s\leqslant 1;\\ \kappa_\delta s, & \text{if } |s|\leqslant\Delta_\delta;\\ -1, & \text{if } -1\leqslant s<-\Delta_\delta,\end{cases}\qquad(16)$$

with $\Delta_\delta$ defined in a natural way as

$$\kappa_\delta\Delta_\delta=f_\delta,\quad\Delta_\delta=\frac{f_\delta}{\kappa_\delta}=\frac{\pi}{2}\delta+O(\delta^2).\qquad(17)$$

It turns out that this approximation gives the right qualitative picture of the signal and is even not too bad quantitatively, providing, for all values $|s|\leqslant 1$, the error within 1/3 for both $\delta=0.3$ and $\delta=0.025$. This accuracy, however, is not enough for the GP-B simulations; moreover, the largest error, associated with the jump of the derivative of function (16) at $s=\pm\Delta_\delta$, occurs in a very sensitive transition region where the fast growth of $F_\delta(s)$ is replaced by its almost constant behavior.

A much more attractive approximation is given by the function

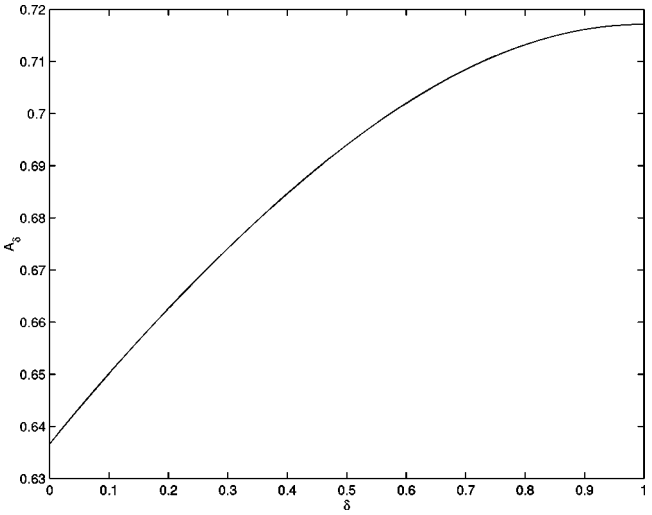


FIG. 3. Dependence of $A_\delta$ on $\delta$.

$$F_\delta(s) \approx \frac{2}{\pi} f_\delta \arctan\left(\frac{\pi}{2}\frac{\kappa_\delta s}{f_\delta}\right), \quad \delta \to +0. \tag{18}$$

The parameters here are arranged in such a way that the slope at $s=0$ is exactly $\kappa_\delta$ and, in the spirit of asymptotic methods, the true saturation value is achieved when $\kappa_\delta s = \infty$ [note that another ''simple and natural'' approximating function, the hyperbolic tangent, is not acceptable, because the rate of approach of $f_\delta$ by $F_\delta(s)$ is a power rather than exponential one]. The performance of the approximation (18) exceeds all expectations, giving, over the whole range of $s$, a maximum error of 20% for $\delta=0.3$, and only 1.8% for $\delta=0.025$. The accuracy is mostly lost outside the transition zone $(-\Delta_\delta, \Delta_\delta)$ due to the fact that $f_\delta$ is achieved only at infinity. This can be dealt with by redefining the parameters to have both the exact slope at $s=0$ and the right value at $s=1$, which produces

$$F_\delta(s) \approx A_\delta \arctan\frac{\kappa_\delta s}{A_\delta}, \quad A_\delta \arctan\frac{\kappa_\delta}{A_\delta} = f_\delta, \quad \delta \to +0. \tag{19}$$

This ''adjusted'' arctan gives the maximum error within 0.3% for $\delta=0.025$; even for as large a separation as $\delta=0.3$ the error is still about 0.6%. Like in Eqs. (16) and (18), the dependence, Eq. (19), is shown in Fig. 2. Coefficient $A_\delta$ is plotted versus $\delta$ in Fig. 3; note the relative flatness of the function.

### D. Closed form expression of the trapped flux

The explicit formula for the trapped flux can also be obtained, although not that easily, from Eq. (11); however, a direct way to get it is to integrate the closed form expression for the magnetic field through the pick-up loop plane $z=0$. For this plane $\vartheta=\pi/2$, $r=\rho$ (the polar radius); in addition, we can redefine $\varphi$ by setting $\varphi_+=0$. Then Eqs. (8) and (3) provide the needed component of the magnetic field in the form

$$B_z|_{z=0} = -\frac{\Phi_0 r_g \cos\vartheta_+}{2\pi}\left[\frac{1}{X^3(\rho,\varphi)} + \frac{\rho - r_g \sin\vartheta_+ \cos\varphi}{2r_g^2 \rho X(\rho,\varphi)\, Y_+(\varphi)\, Y_-(\varphi)} + \frac{\sin\vartheta_+ \cos\varphi}{2r_g^2 \rho\, Y_+(\varphi)\, Y_-(\varphi)} - \frac{1}{2r_g^2 \rho\, Y_-(\varphi)}\right], \tag{20}$$

where

$$X(\rho,\varphi) = \sqrt{r_g^2 - 2r_g\rho\sin\vartheta_+\cos\varphi + \rho^2},$$
$$Y_\pm(\varphi) = 1 \pm \sin\vartheta_+ \cos\varphi. \tag{21}$$

Now we need to integrate Eq. (20) over the area of the pick-up loop. First we calculate the simple, although rather cumbersome, algebraic integral of the field, Eq. (20), times $\rho d\rho$ over the polar radius from 0 to $R$ (if instead, one first integrates over $\varphi$, elliptic integrals of a complicated argument appear in the result that make the closed form radial integration very difficult). As we are then to integrate over the period of $\cos\varphi$, the terms *odd* in $\cos\varphi$ can be omitted, and we obtain

$$\Phi_+(\cos\vartheta_+) = \frac{\Phi_0}{2} F_\delta(\cos\vartheta_+) = -\frac{\Phi_0 r_g \cos\vartheta_+}{2\pi} \times \int_0^{2\pi} d\varphi \left[\frac{R^2 - r_g^2}{2r_g^2 X(R,\varphi)\, Y_+(\varphi)\, Y_-(\varphi)} - \frac{R}{2r_g^2\, Y_-(\varphi)}\right]. \tag{22}$$

In view of Eqs. (21), this integration is also rather straightforward and leads to the desired result,

$$\Phi_+(\cos\vartheta_+) = \frac{\Phi_0}{2}\frac{\cos\vartheta_+}{1-\delta}\left\{\frac{1}{|\cos\vartheta_+|} - \frac{2\delta - \delta^2}{\pi\sqrt{2(1-\delta)(1+\sin\vartheta_+)+\delta^2}} \times \left[\frac{\mathbf{\Pi}(\nu_+,k)}{1+\sin\vartheta_+} + \frac{\mathbf{\Pi}(\nu_-,k)}{1-\sin\vartheta_+}\right]\right\}, \tag{23}$$

where

$$\nu_\pm(\vartheta_+) = \mp\frac{2\sin\vartheta_+}{1\pm\sin\vartheta_+},$$
$$k(\vartheta_+,\delta) = \sqrt{\frac{4(1-\delta)\sin\vartheta_+}{2(1-\delta)(1+\sin\vartheta_+)+\delta^2}}, \tag{24}$$

and $\mathbf{\Pi}(\nu,k)$ is the complete elliptical integral of the third kind (see Ref. 14). As a consistency check, one may calculate the saturation value and the derivative at zero of the transfer function, Eq. (23), to see that they are indeed equal to the previously obtained values, Eqs. (14) and (15).

The first term in Eq. (23) evidently has a jump discontinuity at $s=\cos\vartheta_+=0$. Therefore, for all finite $\delta$, the second term must contain the discontinuity of the opposite sign to make the sum of two analytical in $s$. Hence for small positive $\delta$ in the transition zone we are dealing with a small difference of two large quantities, which is always a problem.

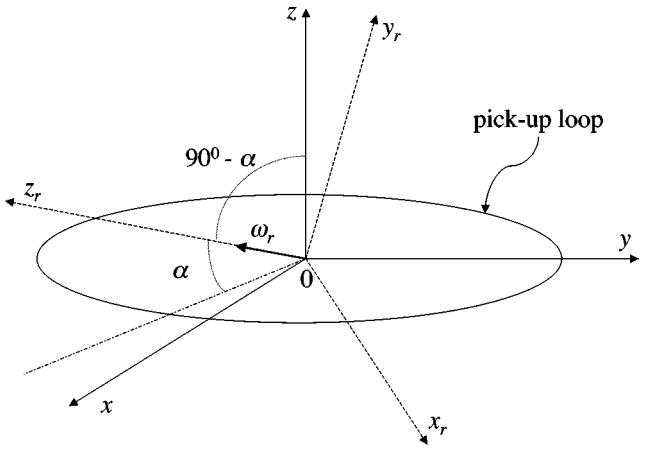


FIG. 4. Mutual orientation of roll and loop coordinates.

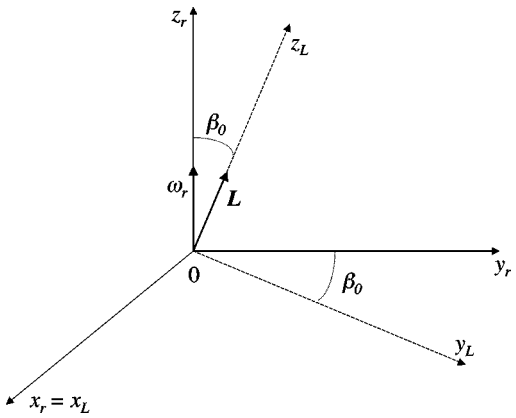


FIG. 5. Mutual orientation of roll and angular momentum coordinates.

Also, the first term in Eq. (23) coincides exactly with expression (12) for $\delta=0$, hence the second one should disappear in this limit, which it necessarily does in a very nonuniform way. Evidently, such an expression cannot be effectively used for both numerical and analytical purposes when $\delta$ is small enough, which is our case.

## IV. FLUXON KINEMATICS AND SPECTRAL DECOMPOSITION OF THE TRAPPED FLUX SIGNAL

Now we need to determine the time signature $\vartheta_+(t)$ of a half-fluxon polar angle in the pick-up loop frame to complete investigation of the trapped flux signal.

In doing that we use four Cartesian coordinate systems. The first one $\{x, y, z\}$ has been introduced in Sec. I; it is fastened to the pick-up loop, and $\mathbf{z}$ is the unit vector normal to the loop plane (Fig. 1). The second coordinate system $\{x_r, y_r, z_r\}$ is associated with the roll axis of the spacecraft, $\hat{\omega}_r = \mathbf{z}_r$ (Fig. 4). The roll axis is almost in the pick-up loop plane, that is, the roll axis—pick-up loop plane misalignment $\alpha \leqslant 10^{-5}$ is very small. The third set of coordinates $\{x_L, y_L, z_L\}$ is related to the angular momentum vector $\mathbf{L}$ in a way that $\mathbf{z}_L = \mathbf{L}/|\mathbf{L}|$. Both the $r$ and $L$ coordinates are fixed in inertial space, since the roll axis is pointed to the Guide Star, and we can so far neglect the pointing errors, as well as the relativistic drift of $\mathbf{L}$. We choose axes $\mathbf{y}_r$ and $\mathbf{y}_L$ in the plane containing both $\mathbf{z}_r$ and $\mathbf{z}_L$, so then the perpendicular to this plane axes $\mathbf{x}_r$ and $\mathbf{x}_L$ coincides (Fig. 5), and the following relations are true:

$$\mathbf{z}_L \cdot \mathbf{z}_r = \mathbf{y}_L \cdot \mathbf{y}_r = \cos\beta_0, \ \mathbf{z}_L \cdot \mathbf{y}_r = -\mathbf{y}_L \cdot \mathbf{z}_r = \sin\beta_0,$$
$$\mathbf{x}_r \cdot \mathbf{z}_r = \mathbf{x}_r \cdot \mathbf{z}_L = \mathbf{x}_r \cdot \mathbf{y}_r = \mathbf{x}_r \cdot \mathbf{y}_L = 0. \tag{25}$$

Here $\beta_0$ is the roll axis—angular momentum misalignment which is required to be $\leqslant 5\times 10^{-5}$ rad in the GP-B experiment.

A symmetric top with the moment of inertia $I+\Delta I$ relative to the body symmetry axis and slightly different value $I$ for the moments of inertia about the other two axes is a very good model for the GP-B rotors (note that $|\Delta I|/I \leqslant 10^{-5}$ for them). Therefore, we choose the fourth Cartesian coordinate system $\{x_B, y_B, z_B\}$ fixed in the rotor's body with $\mathbf{z}_B$ directed along the rotor's symmetry axis.

The dynamics of a symmetric rotor are well known and relatively simple (see Refs. 12 and 13). Its motion in the $L$ coordinates is a precession about $\mathbf{z}_L$ with the spin frequency

$$\omega_s = \frac{L}{I}, \tag{26}$$

and rotation about the rotor symmetry axis $\mathbf{z}_B$ with the frequency

$$\omega_{\text{rot}} = \frac{L}{I+\Delta I}\cos\gamma_B \simeq \omega_s\left(1-\frac{\Delta I}{I}\right)\cos\gamma_B; \tag{27}$$

$0 \leqslant \gamma_B \leqslant \pi$ is the angle between $\mathbf{z}_L$ and $\mathbf{z}_B$.

For the signal of the trapped field we need, however, the time dependence of the position of a source in the inertial coordinates, hence we need expressions of $\mathbf{x}_B(t), \mathbf{y}_B(t), \mathbf{z}_B(t)$ in terms of $\mathbf{x}_L, \mathbf{y}_L, \mathbf{z}_L$. The latter is found with the help of the Euler angles (see, for instance, Ref. 12) in the form

$$\begin{aligned}
\mathbf{z}_B(t) &= \mathbf{z}_L\cos\gamma_B + \mathbf{x}_L\sin\gamma_B\cos\theta_s + \mathbf{y}_L\sin\gamma_B\sin\theta_s,\\
\mathbf{y}_B(t) &= -\mathbf{z}_L\sin\gamma_B\cos\theta_p\\
&\quad + \mathbf{x}_L(\cos\gamma_B\cos\theta_s\cos\theta_p - \sin\theta_s\sin\theta_p)\\
&\quad + \mathbf{y}_L(\cos\gamma_B\sin\theta_s\cos\theta_p + \cos\theta_s\sin\theta_p),\\
\mathbf{x}_B(t) &= -\mathbf{z}_L\sin\gamma_B\sin\theta_p\\
&\quad + \mathbf{x}_L(\cos\gamma_B\cos\theta_s\sin\theta_p + \sin\theta_s\cos\theta_p)\\
&\quad + \mathbf{y}_L(\cos\gamma_B\sin\theta_s\sin\theta_p - \cos\theta_s\cos\theta_p).
\end{aligned} \tag{28}$$

Here the spin and polhode phases are

$$\theta_s(t) = \omega_s t + \theta_s^0, \quad \theta_p(t) = \omega_p t + \theta_p^0, \quad \theta_{s,p}^0 = \text{const}, \tag{29}$$

and $\omega_p$ is a polhode frequency,

$$\omega_p = \frac{L}{I}\frac{|\Delta I|}{I}\cos\gamma_B = \omega_s\frac{|\Delta I|}{I}\cos\gamma_B \tag{30}$$

(in the body-fixed frame the instant angular velocity vector rotates around the rotor's symmetry axis with the polhode frequency). Using this, we obtain the following expression for the unit vector $\mathbf{e}_+$ in the direction of a half-fluxon (i.e., in

the direction of an arbitrary fixed point of the rotor surface at some polar, $0 \leqslant \xi \leqslant \pi$, and azimuthal, $0 \leqslant \eta < 2\pi$, angles in the body-fixed spherical coordinates):

$$\begin{aligned}
\mathbf{e}_+ &= \mathbf{z}_B(t)\cos\xi + (\mathbf{x}_B(t)\cos\eta + \mathbf{y}_B(t)\sin\eta)\sin\xi \\
&\equiv e_1(t)\mathbf{x}_L + e_2(t)\mathbf{y}_L + e_3(t)\mathbf{z}_L\,, \\
e_1(t) &= \sin\xi[\cos\gamma_B\cos\theta_s(t)\sin(\theta_p(t)+\eta) \\
&\quad + \sin\theta_s(t)\cos(\theta_p(t)+\eta)] \\
&\quad + \cos\xi\sin\gamma_B\cos\theta_s(t)\,, \\
e_2(t) &= \sin\xi[\cos\gamma_B\sin\theta_s(t)\sin(\theta_p(t)+\eta) \\
&\quad + \cos\theta_s(t)\cos(\theta_p(t)+\eta)] \\
&\quad + \cos\xi\sin\gamma_B\sin\theta_s(t) \\
e_3(t) &= -\sin\xi\sin\gamma_B\sin(\theta_p(t)+\eta) + \cos\xi\cos\gamma_B\,.
\end{aligned} \tag{31}$$

According to the results of Sec. III, we only need the cosine of the angle $\vartheta_+(t)$ between $\mathbf{e}_+(t)$ and the normal $\mathbf{z}(t)$ to the pick-up loop plane to study the trapped field signal; together with the loop, $\mathbf{z}(t)$ rotates about $\hat{\omega}_r$ with frequency $\omega_r$ (see Fig. 4):

$$\begin{aligned}
\mathbf{z}(t) &= \cos(\pi/2-\alpha)\hat{\omega}_r + \sin(\pi/2-\alpha)(\cos\theta_r\,\mathbf{x}_r + \sin\theta_r\,\mathbf{y}_r) \\
&\equiv \sin\alpha\,\mathbf{z}_r + \cos\alpha\,(\cos\theta_r\,\mathbf{x}_r + \sin\theta_r\,\mathbf{y}_r)\,, \\
\theta_r &= \theta_r(t) = \omega_r t = \text{roll phase}.
\end{aligned} \tag{32}$$

By means of this, Eqs. (31), and formulas (25) relating the $r$ and $L$ coordinates to the first order in the misalignments $\beta_0$ and $\alpha$ we obtain (quadratic and higher order terms are several orders below the required GP-B accuracy):

$$\begin{aligned}
&\cos\vartheta_+(t) = a_{s-r}\sin\Theta_{s-r} + a(\beta_0\sin\theta_r + \alpha), \\
&\Theta_{s-r}(t) = (\omega_s - \omega_r)t + q_{s-r}\,; \quad \theta_r(t) = \omega_r t.
\end{aligned} \tag{33}$$

For a perfectly spherical rotor $\Delta I = 0$ and the amplitudes and initial phase here are true constants whose values depend only on the position of a fluxon relative to the symmetry axis, $a_{s-r} = \sin\xi$, $q_{s-r} = \eta$, $a = \cos\xi$. If, on the other hand, $\Delta I \neq 0$, they start to vary slowly with time at the polhode frequency according to

$$\begin{aligned}
a_{s-r}(\omega_p t) &= \sqrt{[\cos\xi\sin\gamma_B + \sin\xi\cos(\omega_p t + \theta_p^0 + \eta)]^2 + \sin^2\xi\cos^2\gamma_B\sin^2(\omega_p t + \theta_p^0 + \eta)}, \\
\tan q_{s-r}(\omega_p t) &= \frac{\sin\xi\cos\gamma_B\sin(\omega_p t + \theta_p^0 + \eta)}{\cos\xi\sin\gamma_B + \sin\xi\cos(\omega_p t + \theta_p^0 + \eta)}, \\
a(\omega_p t) &= \cos\xi\cos\gamma_B - \sin\xi\sin\gamma_B\sin(\omega_p t + \theta_p^0 + \eta).
\end{aligned} \tag{34}$$

Note that under the conditions of the GP-B experiment the spin frequency is always much larger than the roll and polhode ones, $\omega_r \sim 5\times10^{-5}\omega_s$, $\omega_p \sim 10^{-5}\omega_s$. Since generally the second term in the first equation of Eqs. (33) is about five orders of magnitude smaller than the first one, the input signal for the trapped flux output $\Phi_+(t) = (\Phi_0/2)F_\delta[\cos\vartheta_+(t)]$ is a single carrier harmonics of the (high) spin minus roll frequency ($\Theta_{s-r}$), slowly modulated in the phase and amplitude at polhode frequency, added to by a small dc offset ($\alpha a$) and a small low frequency harmonics ($\theta_r$), both modulated at $\omega_p$. Therefore it is natural and convenient to represent $\Phi_+(t)$ as a Fourier series of spin minus roll harmonics with the amplitudes modulated by low frequencies, namely,

$$\begin{aligned}
\Phi_+(t) &= \frac{\Phi_0}{2}F_\delta(\cos\vartheta_+(t)) \\
&= \frac{\Phi_0}{2}\Bigg[a_{s-r}(\omega_p t)\sum_{k=0}^{\infty}A_k(\omega_p t) \\
&\quad \times\sin(2k+1)\Theta_{s-r}(t) + a(\omega_p t)\,(\beta_0\sin\omega_r t + \alpha) \\
&\quad \times\sum_{k=0}^{\infty}B_k(\omega_p t)\cos 2k\Theta_{s-r}(t)\Bigg];
\end{aligned} \tag{35}$$

$$\begin{aligned}
A_k(\omega_p t) &= \frac{2}{\pi(2k+1)}\int_0^\pi \cos(2k+1)\psi\cos\psi \\
&\quad \times F'_\delta(a_{s-r}(\omega_p t)\sin\psi)\,d\psi + O(\beta_0^2); \\
B_k(\omega_p t) &= \frac{2}{\pi(1+\delta_{k0})}\int_0^\pi \cos 2k\psi \\
&\quad \times F'_\delta(a_{s-r}(\omega_p t)\sin\psi)\,d\psi + O(\beta_0^2);
\end{aligned}$$

here the prime denotes the derivative of $F_\delta(s)$ in $s$.

As readily seen, the amplitudes of *odd* harmonics of $\Theta_{s-r}$ ($A_k$) are generally of the order of unity and decrease as $O(k^{-2})$ for a large enough number $k$. In contrast with that, the amplitudes of *even* harmonics, which are linear in the misalignments, are at least four orders of magnitude smaller but decrease only as $O(k^{-1})$, $k\to\infty$. In addition, the even harmonics are modulated also by the roll frequency $\omega_r$, so that, along with the harmonics $2k\Theta_{s-r}(t)$, $k = 0,1,\ldots$, with amplitudes $\alpha\,a_r(\omega_p t)\,B_k(\omega_p t)$, harmonics $2k\Theta_{s-r}(t) \pm \omega_r t$ are present, whose amplitudes differ only by the misalignment involved, $0.5\beta_0$ instead of $\alpha$.

With all this in mind, one can easily understand that the full spectrum of the trapped flux signal consists of the following series of frequencies: $(2k+1)(\omega_s - \omega_r) \pm m\omega_p$, $2k(\omega_s - \omega_r) \pm \omega_r \pm m\omega_p$ and $2k(\omega_s - \omega_r) \pm m\omega_p$, $m,k$

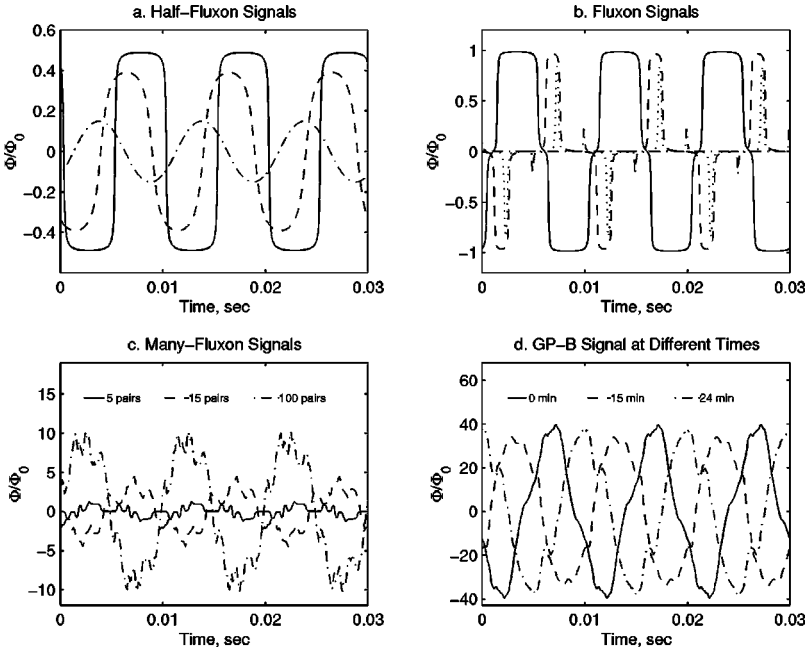


FIG. 6. Simulated readout signals.

$=0,1,\ldots$. The highest peaks are at $(2k+1)(\omega_s-\omega_r)$, and those at $2k(\omega_s-\omega_r)\pm\omega_r$ and $2k(\omega_s-\omega_r)$ are four to five orders of magnitude smaller. All of them are surrounded by an appropriately scaled forest of side bands separated by $\pm m\omega_p$.

The only remaining thing is to discuss briefly the total flux $\Phi$ produced by *all* fluxons. There are always some $N$ fluxons present on the rotor's surface after cooling the rotor down below the transition temperature. Experiments have indicated that the expected number of the pairs is around $N\sim 100$, at most. We denote any values related to either positive or negative half-luxons by indexes $+$ and $-$, respectively, numbering them with the index $i=1,2,\ldots,N$; for instance, their body coordinates will be $\xi^i_+$, $\eta^i_+$ and $\xi^i_-$, $\eta^i_-$, the input signals $S^i_+(t)=\cos\vartheta^i_+(t)$, $S^i_-(t)=\cos\vartheta^i_-(t)$, etc.

The general expression for the total trapped field flux is given by

$$\Phi(t)=\sum_{i=0}^{N}\left[\Phi^i_+(t)+\Phi^i_-(t)\right]$$

$$=\frac{\Phi_0}{2}\sum_{i=0}^{N}\left[F_\delta(\cos\vartheta^i_+(t))-F_\delta(\cos\vartheta^i_-(t))\right]; \quad (36)$$

obviously, the full spectral representation of $\Phi(t)$ is just a scaled up version of $\Phi_+(t)$ given in Eqs. (35).

Since for small $\delta$ the transfer function $F_\delta(s)$ is close to $\pm F_\delta(1)\approx\pm 1$ everywhere except within a small vicinity of the origin (see Sec. III), expressions (36) and (35) demonstrate that the maximum value of $\Phi(t)$ is distributed according to the usual counting statistics, provided that the distribution of fluxons over the surface of the rotor is a uniform random one. Therefore $N$ fluxons in this case should produce a total flux on the order of $\sqrt{N}\Phi_0$ for ''large'' $N$.

## V. CODE AND SIGNAL ANALYSIS

For the GP-B error analysis and data reduction one needs to simulate the trapped flux signal as expected in the SQUID output. To do that, the results obtained earlier were utilized for writing a program that is able to be fast enough to generate, store, and analyze the high-frequency signal. The code, written in the MATLAB V.5.0 to ensure compatibility with other GP-B software, is available from the authors.

The program is very versatile, allowing many options and many different tasks. For instance, there may be a different *number of fluxons*, and their *positions* may be read either from a prewritten file or generated at random according to different probability distributions. *Transfer function* may be calculated by means of several different expressions introduced in Sec. III. Generation of the *high frequency signal* and/or its slow varying *Fourier amplitudes*, Eqs. (35) and (36), is possible. In addition, all gyroscope and pick-up loop parameters (radii, rotor asphericity, misalignments, etc.), as well as the discretization frequency, time intervals, and all angular velocities may be specified in an arbitrary way.

A lot of attention in the program's realization has been paid to the fact that tracing positions of as much as 100 fluxons for long enough periods of time with high discretization frequency easily becomes too memory consuming. The program has thus been optimized in several directions, so as to not cause excessive memory swaps to the hard drive and not lead to the memory fragmentation, and to access the hard drive for data storage as infrequently as possible. The following data may be useful to estimate the code's speed: on a Sun UltraSparc 5 with 128 megabytes of random access memory (RAM) running System V, Rel. 4.0 and having a network mounted storage drive it takes, depending on the network load, from 1.5 up to 2 h to generate 1 h of signal of

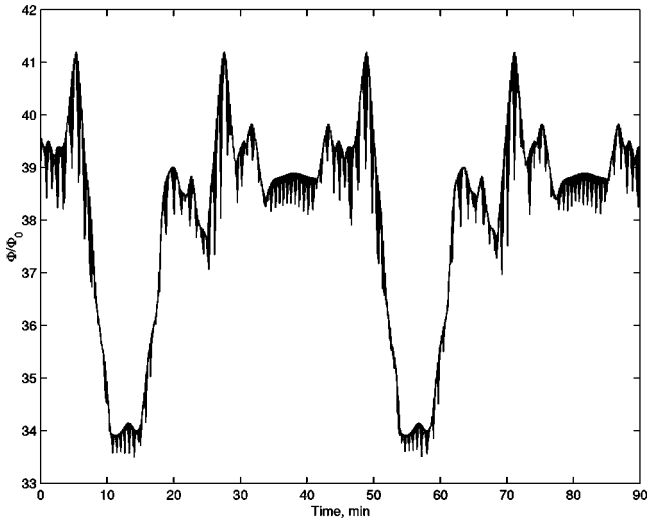


FIG. 7. Envelope of the simulated trapped flux signal, $T_p \approx 43.6$ min.

100 fluxons at a sampling frequency of 2200 Hz (the actual sampling rate of GP-B electronics).

We will not elaborate more here on the code details but will continue with the results of our simulations. All of them have been performed with the parameters set at the values expected for the GP-B experiment (see cf. Refs. 1–3). In particular, the spin frequency $f_{\text{spin}}=100$ Hz, the roll period $T_r=3$ min, the polhode period $T_p \approx 43.6$ min; recall that $\delta = 0.025$.

In Fig. 6 the signals are seen as generated by different number of fluxons distributed in various ways over the surface of the gyroscope. In all of the graphs the ''adjusted arctan'' approximation (19) to the universal curve is used. Figure 6(a) shows signals of a positive half-fluxon (without its negative counterpart) positioned at different points on the gyro. The majority of magnetic charge positions provide signals like the one drawn as a solid line. The dashed and dash-dotted lines correspond to rare charges oscillating in a small ($\sim \Delta_\delta$) vicinity of the pick-up loop plane, which is why their amplitude is smaller. On average, one cannot expect too many charges like that, however, each of the four GP-B rotors will carry just one *particular* realization of the fluxon position distribution, so these ''weak'' half-fluxons are possible.

Figure 6(b) shows various signals from one fluxon. Again, the solid line corresponds to ''the most probable'' signal: the positive and negative half-fluxons are far from each other (although not opposite on the sphere) and have large oscillation amplitudes.

Figure 6(c) shows typical signals of 5, 15, and 100 fluxons distributed *randomly* with the *uniform* probability over the gyro's surface. The $\sqrt{N}$ growth of the signal is visible; the complexity of the signal profile also clearly increases with $N$.

Figure 6(d) shows short fragments of the 12 h of signal generated for the test of the GP-B data reduction algorithms. There are 100 fluxons distributed unevenly: 60 of them are uniformly spread at random over the surface [just like in Fig. 6(c)], while the remaining 40 are used to create a total net flux of $\sim 40\,\Phi_0$ along some random axis. This should account for the small residual magnetization of the rotor at the time when it was made superconducting (see Ref. 17). This magnetization not only significantly increases the amplitude of the signal, it also smoothes it out. Different curves in Fig. 6 correspond to the signals taken at different stages of the polhoidal motion (namely, 0, 15, and 24 min from some reference point) for a duration of three spin periods.

In Fig. 7 a low-frequency envelope is plotted of the signal from Fig. 6(d) used in the GP-B simulations. The graph was constructed by splitting the magnetic flux signal into 2 s blocks (4400 data points in each) and plotting the maximum value of the flux for each block. The periodicity of the large scale structures of the envelope with an approximate polhode period of about 43 min is clear. On the other hand, a comparison of the signal in any two corresponding regions demonstrates that the short scale features, presumably introduced by the roll frequency and other less intensive harmonics, are not repeated precisely every polhode period $T_p$, which is expected because $T_p$ and the roll period $T_r$ are incommensurable.

Figure 8 shows the slow polhoidal variation of Fourier amplitudes of the spin minus roll harmonics calculated according to Eqs. (35) and summed over the fluxons. The first 10 odd and even harmonics are shown in plots (a) and (b), respectively, in Fig. 8. Recall that in expressions (35) for the flux all even harmonics are multiplied by the misalignments, so that the actual vertical scale in Fig. 8(b) is about $10^5$ that in Fig. 8(a). The pictures clearly show that the odd harmon-

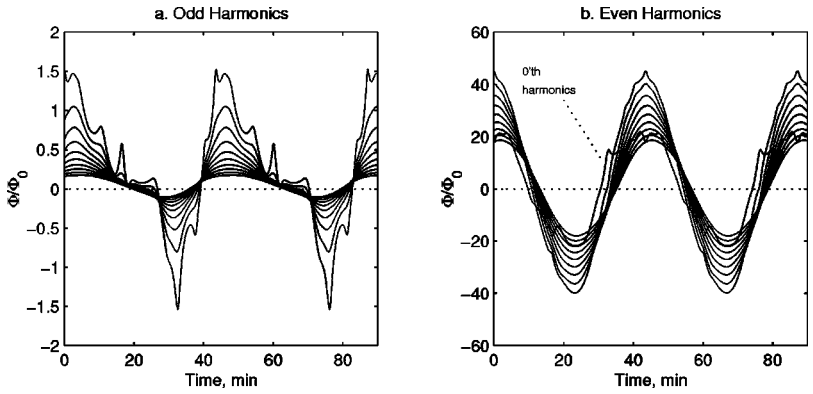


FIG. 8. Slowly varying amplitudes of the Fourier harmonics of the trapped flux signal, $T_p \approx 43.6$ min.

ics drop much faster with the number than the even ones, as predicted. It is interesting to note that the lowest even ($n=0$) harmonics, which gives the amplitude of the dc and the roll frequency components, has a shape rather distinctive from the profile of the other modes.

## ACKNOWLEDGMENTS

This work was supported by NASA Grant No. NAS 8-39225 to Gravity Probe B. The authors are grateful to Dr. G. M. Keiser, who had originally initiated this work, Dr. M. Heifetz for many valuable comments, and to the Gravity Probe B Theory group for fruitful discussions.

## APPENDIX: SUMMATION OF CERTAIN SERIES OF LEGENDRE POLYNOMIALS

Here we give a derivation of formulas (14) and (15) for $f_\delta = F_\delta(1)$ and for the slope $\kappa_\delta$ of the transfer function at $s=0$. We use the Pochgammer symbol $(\alpha)_0=1$, $(\alpha)_k=\alpha(\alpha+1)\ldots(\alpha+k-1)=\Gamma(\alpha+k)/\Gamma(\alpha)$, as well as the standard notation,

$$F(a,b,c;\zeta)=\sum_{k=o}^{\infty}\frac{(a)_k(b_k)}{(c)_k}\frac{\zeta^k}{k!},$$

for the Gauss hypergeometric function of argument $\zeta$ and parameters $a$, $b$, and $c$. From Eq. (11) we have

$$F_\delta(s)\equiv F_\delta^{(1)}(s)-F_\delta^{(2)}(s);$$

$$F_\delta^{(1)}(s)=2\eta\sum_{k=0}^{\infty}\frac{(-\eta^2)^k}{k!}\left(\frac{1}{2}\right)_k P_{2k+1}(s), \tag{A1}$$

$$F_\delta^{(2)}(s)=\frac{\eta}{2}\sum_{k=0}^{\infty}\frac{(-\eta^2)^k}{(k+1)!}\left(\frac{1}{2}\right)_k P_{2k+1}(s),$$

where we introduced $\eta=1-\delta$ for brevity.

### A. Calculation of $f_\delta$

Since $P_n(1)=1$, we have

$$F_\delta^{(1)}(1)=2\eta\sum_{k=0}^{\infty}\frac{(-\eta^2)^k}{k!}\left(\frac{1}{2}\right)_k=\frac{2\eta}{\sqrt{1+\eta^2}};$$

$$F_\delta^{(1)}(1)=\frac{\eta}{2}\sum_{k=0}^{\infty}\frac{(-\eta^2)^k}{(k+1)!}\frac{(\frac{1}{2})_k(1)_k}{(2)_k}=\frac{\eta}{2}F(1/2,1,2;-\eta^2)=\eta^{-1}(\sqrt{1+\eta^2}-1),$$

and for the elementary expression of the hypergeometric function we have used formula (11) from Ref. 15 (2.11) with $a=1/2$ and $b=1$. Combining these results with Eqs. (A1), we obtain

$$f_\delta=F_\delta(s)=F_\delta^{(1)}(s)-F_\delta^{(2)}(s)=\frac{2\eta}{\sqrt{1+\eta^2}}-\frac{\sqrt{1+\eta^2}-1}{\eta}=\frac{1}{\eta}\left(1-\frac{1-\eta^2}{\sqrt{1+\eta^2}}\right),$$

which, in view of $\eta=1-\delta$, is exactly the same as expression (14).

### B. Calculation of $\kappa_\delta$

As [see Ref. 15 (10.10), (12)]

$$P'_{2k+1}(0)=(2k+1)\,P_{2k}(0)=\frac{(-1)^k}{k!}\left(\frac{3}{2}\right)_k,$$

from Eqs. (A1) we find

$$\left.\frac{\partial F_\delta^{(1)}}{\partial s}\right|_{s=0}=2\eta\sum_{k=0}^{\infty}\frac{(-\eta^2)^k}{k!}\left(\frac{1}{2}\right)_k P'_{2k+1}(0)=2\eta\sum_{k=0}^{\infty}\frac{(\eta^2)^k}{k!}\frac{(\frac{1}{2})_k(\frac{3}{2})_k}{(1)_k}=2\eta F(1/2,3/2,1;\eta^2)=\frac{2\eta}{1-\eta^2}F(1/2,-1/2,1;\eta^2)=\frac{4\eta}{\pi(1-\eta^2)}\mathbf{E}(\eta), \tag{A2}$$

where $\mathbf{E}(\eta)$ is the complete elliptical integral of the second kind, and we have exploited the classical relation [see Ref. 15 (2.1.4), (23)]

$$F(a,b,c;\zeta)=(1-\zeta)^{c-a-b}F(c-a,c-b,c;\zeta),$$

and the expression for the elliptical integral in terms of the hypergeometric function [see Ref. 16 (13.8)] is

$$F(1/2,-1/2,1;\eta^2)=\frac{2}{\pi}\mathbf{E}(\eta). \tag{A3}$$

Similarly,

$$\left.\frac{\partial F_\delta^{(2)}}{\partial s}\right|_{s=0}=\frac{\eta}{2}\sum_{k=0}^{\infty}\frac{(-\eta^2)^k}{(k+1)!}\left(\frac{1}{2}\right)_k P'_{2k+1}(0)=\frac{\eta}{2}\sum_{k=0}^{\infty}\frac{(\eta^2)^k}{k!}\frac{(\frac{1}{2})_k(\frac{3}{2})_k}{(2)_k}=\frac{\eta}{2}F(1/2,3/2,2;\eta^2)=\frac{\eta}{2}(-4)\frac{d}{d(\eta^2)}F(-1/2,1/2,1;\eta^2)=\frac{-4\eta}{\pi}\frac{d}{d(\eta^2)}\mathbf{E}(\eta)=-\frac{2}{\pi\eta}[\mathbf{E}(\eta)-\mathbf{K}(\eta)], \tag{A4}$$

and here we used the formula for the derivative of the hypergeometric function [see Ref. 15 (2.8), (20)], formula (A3) again, and a formula for the derivative of $\mathbf{E}(\eta)$ [see Ref. 16 (13.7), (12)]; $\mathbf{K}(\eta)$ is the complete elliptic integral of the first kind.

Equations (A2) and (A4) now provide

$$\kappa_\delta = \left.\frac{\partial F_\delta}{\partial s}\right|_{s=0} = \left.\frac{\partial F_\delta^{(1)}}{\partial s}\right|_{s=0} - \left.\frac{\partial F_\delta^{(2)}}{\partial s}\right|_{s=0}$$
$$= \frac{2}{\pi\eta}\left[\frac{1+\eta^2}{1-\eta^2}\mathbf{E}(\eta) - \mathbf{K}(\eta)\right],$$

which coincides with the exact expression in Eq. (15); the asymptotic formula there for small $\delta = 1-\eta$ is obtained by using the expansions of elliptical integrals in the series in the conjugate modulus [see Ref. 14 (773.3), (774.3)].

[1] J. P. Turneaure *et al.*, Adv. Space Res. **9**, 29 (1989).
[2] S. Buchman *et al.*, in *Proceedings of the 7th Marcel Grossman Meeting on General Relativity*, edited by R. T. Jantzen and G. M. Keiser (World Scientific, Singapore, 1996), Part B, p. 1533.
[3] B. Muhlfelder *et al.* in Ref. 2, p. 1545.
[4] C. W. F. Everitt, in *Near Zero*, edited by J. D. Fairbank, B. S. Deaver, Jr., C. W. F. Everitt, and P. F. Michelson (Freeman, New York, 1988), p. 685.
[5] G. M. Keiser, in Ref. 2, p. 207.
[6] F. London, *Superfluids* (Dover, New York, 1961), Vol. 1.
[7] M. Tinkham, *Introduction to Superconductivity* (McGraw–Hill, New York, 1996), Chaps. 5.
[8] L. Landau and E. Lifshitz, *Electrodynamics of Continuous Media*, 2nd ed. (Pergamon, Oxford, 1984), Chap. 4.
[9] A. C. Rose-Innes and E. H. Rhoderick, *Introduction to Superconductivity* (Pergamon, Oxford, 1978), Chap. 12.
[10] L. L. Wai, BS honors thesis, Dept. of Physics, Stanford University, 1989.
[11] H. Bateman and A. Erdélyi, *Higher Transcendental Functions*, (McGraw–Hill, New York, 1953), Vol. 2.
[12] L. Landau and E. Lifshitz, *Mechanics* (Pergamon, Oxford, 1959).
[13] H. Goldstein, *Classical Mechanics* (Addison–Wesley, Reading, MA, 1950).
[14] H. B. Dwight, *Tables of Integrals and Other Mathematical Data*, 4th ed. (Macmillan, New York, 1961), Chap. IX.
[15] H. Bateman and A. Erdélyi, in Ref. 11, Vol. 1.
[16] H. Bateman and A. Erdélyi, in Ref. 11, Vol. 3.
[17] G. T. Haupt, Ph.D. thesis, Dept. of Aeronautics and Astronautics, Stanford University, 1989.